Structural dynamics of surfaces by ultrafast electron crystallography: Experimental and multiple scattering theory

Sascha Schäfer, Wenxi Liang, and Ahmed H. Zewail

Citation: J. Chem. Phys. **135**, 214201 (2011); doi: 10.1063/1.3663963
View online: http://dx.doi.org/10.1063/1.3663963
View Table of Contents: http://jcp.aip.org/resource/1/JCPSA6/v135/i21
Published by the American Institute of Physics.

Structural dynamics of surfaces by ultrafast electron crystallography: Experimental and multiple scattering theory

Sascha Schäfer, Wenxi Liang, and Ahmed H. Zewail[a)]
Physical Biology Center for Ultrafast Science and Technology, Arthur Amos Noyes Laboratory of Chemical Physics, California Institute of Technology, Pasadena, California 91125, USA

(Received 1 September 2011; accepted 2 November 2011; published online 2 December 2011)

Recent studies in ultrafast electron crystallography (UEC) using a reflection diffraction geometry have enabled the investigation of a wide range of phenomena on the femtosecond and picosecond time scales. In all these studies, the analysis of the diffraction patterns and their temporal change after excitation was performed within the kinematical scattering theory. In this contribution, we address the question, to what extent dynamical scattering effects have to be included in order to obtain quantitative information about structural dynamics. We discuss different scattering regimes and provide diffraction maps that describe all essential features of scatterings and observables. The effects are quantified by dynamical scattering simulations and examined by direct comparison to the results of ultrafast electron diffraction experiments on an *in situ* prepared Ni(100) surface, for which structural dynamics can be well described by a two-temperature model. We also report calculations for graphite surfaces. The theoretical framework provided here allows for further UEC studies of surfaces especially at larger penetration depths and for those of heavy-atom materials. © *2011 American Institute of Physics*. [doi:10.1063/1.3663963]

I. INTRODUCTION

Ultrafast electron diffraction experiments have given valuable insights into the temporal evolution of dynamical processes on a structural level.[1–3] Since the early experiments the field has already developed into several branches including transmission electron diffraction (TED),[4–7] and ultrafast electron diffraction in a reflection geometry (ultrafast electron crystallography, UEC).[8,9] Ultrafast electron microscopy (UEM), besides diffraction, enables real-space and spectrum imaging.[10–13] The unique feature of electron diffraction in a reflection geometry is the high surface sensitivity due to the large scattering cross-section of electrons with matter and the grazing incidence of the setup. Both factors combined enable UEC to probe the surface and the first few nanometers within the sample, permitting the study of femtosecond surface, interface, and adsorbate dynamics which are hardly accessible in TED or UEM.

However, the strong scattering between the probing electrons and the surface leads to multiple scattering (also called: dynamical scattering) effects which are not accounted for in simple kinematical scattering theory. This is long known in static reflection high energy electron diffraction (RHEED) at surfaces and theoretical tools have been developed to describe the resulting diffraction patterns in the presence of strong multiple scatterings (see, e.g., Refs. 14–16).

In previous UEC experiments, time-dependent changes in an electron diffraction pattern were analyzed and discussed within the framework of kinematical diffraction theory. As the UEC method became more mature and more widely applied it seems natural to ask, to what extent multiple scattering effects have to be incorporated in the experimental analysis, what qualitative features do they exhibit, and whether it is possible to extract quantitative structural dynamics from UEC experiments once a proper multiple scattering theory is applied.

In this contribution, we address these points by developing a dynamical scattering methodology. Using this approach, we compare the simulated diffraction pattern changes of a Ni(100) surface to the experimental results. While the dynamical scattering approach gives temporal diffraction pattern changes in good agreement with experiment, relatively large discrepancies are observed when the kinematical scattering theory is used. Furthermore, we give a qualitative framework to discuss these discrepancies using the concepts of Bragg reflections and surface wave resonances. Finally, we also apply the dynamical scattering analysis to excitation-induced dynamics in graphite to elucidate what additional effects occur in highly anisotropic, low-Z materials.

II. EXPERIMENTAL METHODS

The experimental setup of the Caltech UEC experiments has already been described in detail elsewhere.[1,17] Briefly, the apparatus consists of a sample preparation chamber equipped with standard surface preparation tools, a load lock chamber and a third chamber which contains the actual UEC compartment.

Here, an electron pulse with an energy per particle of 30 keV and sub-ps pulse width is generated in a photoelectron gun[4,18,19] and focussed onto the sample in grazing incidence. The sample is mounted on a 5-axis goniometer, so that the incidence angle of the electron beam onto to sample and its azimuthal angle relative to a zone axis of the sample can be adjusted. The electron pulse gets diffracted at the sample

a)Author to whom correspondence should be addressed. Electronic mail: zewail@caltech.edu.

surface and the diffraction pattern is detected by a phosphor-screen/CCD assembly, which is capable of single-electron detection.

To record ultrafast dynamics, the sample is excited by a femtosecond laser pulse (1 kHz, 100 fs, 800 nm) and the subsequent change of the diffraction pattern is detected by varying the time delay between the electron and the laser pulse. The difference in the arrival time of the electron pulse at different parts of the sample is compensated for by tilting the wavefront of the optical excitation pulse relative to its propagation direction,[20] which was shown to give sub-ps time-resolution.[9] The fluence of the excitation laser at the sample position was calibrated by scanning a knife edge across the beam profile and recording the passing residual pulse energy.

In the grazing-angle geometry, it is known[1,21,22] that under special conditions not only structural dynamics but also transient electric field effects can lead to a temporal change of the detected diffraction pattern on a 10–100 ps time scale. However, by recording the time-dependent movement of a tangential electron beam in the similar case of adsorbate covered nickel samples (Ni(100)-c(2×2)-S) we find negligible transient electric fields.[23] Furthermore, for the case of nickel reported here we only observe diffraction intensity changes which are not sensitive to transient electric fields. The preparation of the nickel sample and its characterization is described in Appendix A.

III. THEORETICAL METHODS

A. Dynamical diffraction theory

Due to the high scattering cross-section between electrons and matter there is a substantial probability that an incident electron is scattered several times before it leaves the sample.[14–16]

In order to calculate the intensities of diffracted electron beams into different directions we have to analyze the physical situation depicted in Fig. 1. An electron beam with a wave vector $\boldsymbol{k}_0$, described by a wave function $\Psi_+ = A_0 \exp(i\boldsymbol{k}_0 \cdot \boldsymbol{r})$, is impinging on a sample from the upper half space. Here, $\boldsymbol{r}$ denotes the electron position. The spatially varying scattering potential inside the sample leads to a set of new beams $A_i' \exp(i\boldsymbol{k}_i' \cdot \boldsymbol{r})$ in the half space below the sample and a set of counter propagating beams $A_i'' \exp(-i\boldsymbol{k}_i'' \cdot \boldsymbol{r})$ above the sample. Thus the wave function of the scattered electron in the upper half space (near-field) is $\Psi_u = \Psi_+ + \Psi_-$ with $\Psi_- = \sum_i A_i'' \exp(-i\boldsymbol{k}_i'' \cdot \boldsymbol{r})$; similarly, the wave function in the lower half space is given by $\Psi_l = \Psi_+' = \sum_i A_i' \exp(i\boldsymbol{k}_i' \cdot \boldsymbol{r})$. It is the intensities of the counter propagating beams (in the far-field), $I_i = A_i''^* A_i''$, for different momenta of the incident beam, $\boldsymbol{k}_0$, which are experimentally detected in a reflective diffraction setup. The transmitted beams are usually not observed in a reflection setup, since the mean-free-path of 30 kV electrons is on the order of 100 nm, which is much smaller than a typical sample thickness (~1 mm). Nevertheless, transmitted beams have to be included in the theoretical simulation, since an electron can be first scattered in the forward direction and subsequently backscattered creating a diffracted beam in reflection. The thickness of the model slab is increased until the intensity of the reflected electrons no longer change. In the following it is assumed that the incident electron is only elastically scattered, i.e., when $\boldsymbol{k}_0^2 = \boldsymbol{k}_i'^2 = \boldsymbol{k}_i''^2$. Normally in UEC the energy of the incident electron is held constant, i.e., $|\boldsymbol{k}_0| = \text{const.}$, but its direction relative to the sample is changed.

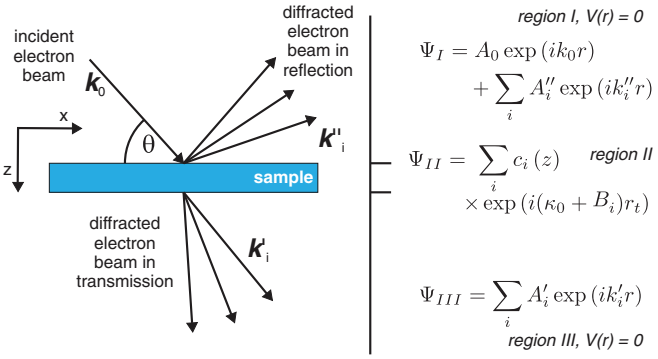

FIG. 1. Schematics of the diffraction geometry. An electron beam with wave vector $\boldsymbol{k}_0$ impinges on the sample with an incidence angle θ. Due to the scattering potential within the sample a set of diffracted electron beam is generated in transmission ($\boldsymbol{k}_i'$) and reflection ($\boldsymbol{k}_i''$). Above and below the sample the scattering potential V is zero and the wave function is a superposition of non-interacting plane waves. Inside the sample the wave function can be described by using a 2D-Bloch wave approach.

In order to calculate A_i'' the Hamiltonian $\mathcal{H}$ of the scattered electron is considered, which is, to a good approximation, a one-particle Hamiltonian of the form $\mathcal{H} = -\hbar^2/(2m_e)\nabla^2 + V(\boldsymbol{r})$. Solving the Schrödinger equation with the boundary conditions, that the only wave propagating in the positive z-direction in the upper half space is given by Ψ_+ and, furthermore, that there is no wave propagating in the negative z-direction in the lower half space, gives the full wave function of the electron, and thus the coefficients A_i''.

In the limit that the scattering potential exerts only a weak perturbation (single scattering) on the incident electron beam, we can analytically express A_i'' by employing the Born approximation[14] which gives the kinematical scattering approximation:

$$A_i'' = \text{const.} \times \int V(\boldsymbol{r}) \exp(-i(\boldsymbol{k}_i'' - \boldsymbol{k}_0) \cdot \boldsymbol{r}) d\boldsymbol{r}. \qquad (1)$$

In this case the intensities, $A_i''^* A_i''$, of the diffracted beams can be obtained from the Fourier-transform of the scattering potential which, in turn, is related to the structure of the sample. Thus, the diffraction pattern and its change, for the case of time-resolved diffraction, are directly connected to structure and structural change, provided that only single scattering events occur.

However, to incorporate multiple scattering events we cannot rely on the Born approximation and have to numerically solve the Schrödinger equation. For this purpose, we implemented a parallel-to-surface multislice algorithm as described by Ichimiya.[24] The correct implementation was verified by comparison to reported results of multiple scattering calculations for Ag(100) surfaces,[25] and a comparison of different numerical approaches can be found in the literature.[14] In the algorithm which is employed in this work the scattering problem is solved in a mixed real-space/Fourier-space

approach. It is assumed that the potential $V(\boldsymbol{r})$ is periodic in directions tangential to the surface of the sample, so that the electron wave function can be written as Bloch waves in these directions, i.e., as

$$\Psi = \sum_i c_i(z) \exp\left(i(\boldsymbol{\kappa}_0 + \boldsymbol{B}_i) \cdot \boldsymbol{r}_t\right), \tag{2}$$

where $\boldsymbol{\kappa}_0$ and $\boldsymbol{r}_t$ are the tangential components of $\boldsymbol{k}_0$ and $\boldsymbol{r}$. $\boldsymbol{B}_i$ is a vector of the reciprocal surface net, with i indexing all reciprocal net points. Taking $\boldsymbol{a}^*$ and $\boldsymbol{b}^*$ as the reciprocal unit mesh vectors gives $\boldsymbol{B}_i = h\boldsymbol{a}^* + k\boldsymbol{b}^*$ with integer numbers h and k.

For $z \to -\infty$, the individual summands in Eq. (2) relate to the eventually detected beams outside of the sample with a tangential momentum component of $\boldsymbol{\kappa}_0 + \boldsymbol{B}_i$. The corresponding momentum component Γ_i perpendicular to the surface is given by $\Gamma_i^2 = \boldsymbol{k}_0^2 - (\boldsymbol{\kappa}_0 + \boldsymbol{B}_i)^2$, due to energy conservation.

The Bloch wave ansatz Eq. (2) transforms the Schrödinger equation into a system of ordinary second order differential equations for $c_i(z)$. To obtain a numerical tractable problem, the number of indices i has to be truncated at a finite number of points on the reciprocal surface net. Care has to be taken that the finite number of chosen points are leading to converged solutions of the scattering problem. It turns out that a sufficient number of reciprocal lattice points in the zero order Laue zone, i.e., with $\boldsymbol{B}_i \cdot \boldsymbol{k}_0 = 0$, are necessary. Higher order Laue zones only give small corrections.[26] In the calculations reported here, 33 reciprocal lattice points were included.

The truncated, finite system of differential equations is finally solved by discretizing z into small steps Δz, giving a system of linear eigenequations in each step. Numerically solving these eigenequations and matching their solutions inside the sample as well as to the above mentioned boundary conditions above and below the sample gives the coefficients $c_i(z)$ and thus the amplitudes A_i''.

In order to define the Hamiltonian, the potential $V(\boldsymbol{r})$, which the scattered electron experiences within the solid, has to be known. In a common approximation, which we also adopt in this work, $V(\boldsymbol{r})$ is assumed to be a superposition of element-specific atomic potentials $V_L(\boldsymbol{r} - \boldsymbol{r}_L)$ such that $V(\boldsymbol{r}) = \Sigma_L V_L(\boldsymbol{r} - \boldsymbol{r}_L)$, where the summation runs over all atoms L at positions $\boldsymbol{r}_L$. The atomic potentials V_A are derived from the atomic scattering factors, parametrized by the tabulated Doyle-Turner coefficients.[27] This approach neglects bonding effects on the potential $V(\boldsymbol{r})$ that can be studied by, e.g., convergent beam electron diffraction.[28] However, it has been shown that already a satisfactory agreement between theoretical predictions and experiments can be achieved by using an element-specific atomic potential.[14]

The Hamiltonian $\mathcal{H}$ as defined above conserves the norm of the wave function, but it is necessary to include absorption effects which damp the coherent electron wave within the solid. This is done by adding an imaginary component $i\,V_i(\boldsymbol{r})$ to the potential. Choosing $V_i(\boldsymbol{r}) = 0.1 \times V(\boldsymbol{r})$ was shown to reproduce the basic features introduced by electron absorption, although it is known that the actual imaginary potential due to thermal diffuse and plasmon scattering has a different shape than the real part of the scattering potential.[29]

We note that this approach does only account for the decreasing intensity of elastically scattered electrons but does not describe diffraction due to inelastically scattered electrons. In the case of phonon scattering the inelastically scattered electrons predominantly form a diffuse background in the experimentally observed diffraction pattern, where, again, dynamical scattering effects have to be carefully considered.[30,31] The photo-induced ultrafast changes of the background intensity are not discussed in this contribution and their useful information (see, e.g., Ref. 32) will be discussed elsewhere.[33] Finally, the use of the Bloch-wave ansatz for the wave function does not take into account surface disorders such as monoatomic steps.

B. The two-temperature model and structural dynamics of Ni(100)

We begin here by comparing the experimentally obtained structural dynamics of the Ni(100) surface to the dynamics predicted by a two-temperature model (TTM)[34] as a theoretical reference point. In this model, the electronic and vibrational subsystems are each in a local equilibrium state defined by the temperature $T_e(z, t)$ and $T_l(z, t)$, respectively.[35] The temporal and spatial change of T_e and T_l is given by

$$\begin{aligned} C_e \frac{\partial T_e}{\partial t} &= \frac{\partial}{\partial z} \kappa_e \frac{\partial T_e}{\partial z} - g(T_e - T_l) + S(z, t), \\ C_l \frac{\partial T_l}{\partial t} &= g(T_e - T_l), \end{aligned} \tag{3}$$

where κ_e denotes the electronic heat conductivity,[36] C_e and C_l are the electron and lattice heat capacities, and g is the electron-phonon coupling constant.

The initial rate of increase of the electronic energy due to laser excitation is denoted by $S(z, t)$ and is given by

$$S(z, t) = \frac{(1 - R)\,F}{\chi} \exp(-z/\chi)\, \frac{\operatorname{sech}^2(t/\tau)}{2\tau}, \tag{4}$$

where the first two terms describe the optical properties of the sample and the last term signifies the temporal profile of the excitation laser pulse. For nickel, $R = 0.68$ is the reflectivity of the surface, $\chi = 14$ nm, the penetration depth of the excitation laser,[37] and τ is related to the laser pulse width through $\tau = 100\,\text{fs}/1.76$. F denotes the fluence of the excitation laser. By using the optical penetration depth χ in describing the spatial excitation profile, we neglect the contribution of ballistic electron transport. This is justified if the mean free path of excited electrons is smaller than the optical penetration depth. Previous studies have pointed out the importance of ballistic transport, e.g., in ultrafast heating of gold films where the electron mean free path can be as large as ~100 nm.[38] However, for the case of nickel, the mean-free-path of electrons at room temperature is estimated to be only 11 nm.[38] Furthermore, at elevated temperatures after laser excitation, increased electron-electron and electron-phonon scattering will lead to an additional decrease of the mean free path compared to its room temperature value. Therefore, we expect that ballistic electron transport only gives a minor contribution to the initial spatial spread of the excitation energy in nickel.

To obtain the spatial and temporal evolution of T_e and T_l, we solved Eq. (3) numerically. As it is shown below, the electron predominantly scatters within the first 1–2 nm of the sample surface. Over this distance, T_e and T_l do not change considerably and can be well approximated by the corresponding temperatures $T_e(0, t)$ and $T_l(0, t)$ directly at the surface.

Recently, it has been pointed out that for many transition metals it is necessary to include the temperature dependence of the material constants in Eq. (3) to accurately describe the heating and cooling dynamics after femtosecond laser excitation.[39,40] Therefore, we use the temperature-dependent values, $C_e(T_e)$, $C_l(T_l)$, $g(T_e)$, and $\kappa_e(T_e, T_l)$ as reported in Ref. 39, to incorporate these effects.

For time scales much longer than C_e/g, T_e, and T_l become asymptotically equal and an analytical solution can be found for this limit,[41]

$$\Delta T(0,t) = \Delta T_0 \exp\left(\frac{\kappa t}{\chi_0^2}\right) \operatorname{erfc}\sqrt{\frac{\kappa t}{\chi_0^2}} \approx \Delta T_0 \sqrt{\frac{\chi_0^2}{\pi \kappa t}}, \qquad (5)$$

which predicts that the cooling dynamics of the surface follows a $1/\sqrt{t}$ behavior.

The temporal and spatial change of T_e and T_l, as obtained from the two-temperature model, can be used to construct a simple description of the structural dynamics of the lattice for which we consider the temporal and spatial change of the perpendicular unit cell dimension c and of the atomic mean square displacement $\Delta\langle u^2\rangle$. Because the lattice system can be described by a temperature T_l, the dynamical evolution of $\Delta\langle u^2\rangle$ can be expressed using the equilibrium-like expression $\Delta\langle u^2\rangle = 9\hbar^2/(mk_b\theta_D^2)\Delta T_l$ (m: atomic mass Ni; $\theta_D = 370$ K: Debye temperature of nickel, reproducing the experimental mean square displacement[42,43]).

For the temporal change of the (perpendicular) unit cell dimension we use a one-dimensional chain-model[44–47] where each chain node corresponds to an atomic layer parallel to the surface. The layers are connected to the neighboring layers by harmonic springs with a uniform spring constant per atom, k_s, which can be derived from the longitudinal sound velocity $v = 5277$ m/s[37] by using $k_s = m(2v/c_0)^2$ (equilibrium layer distance $c_0/2 = 1.76$ Å).

The equilibrium distance, d_i, i.e., the minimum of the harmonic potential, between the ith and $(i + 1)$th layer is a function of the electron and lattice temperature,

$$d_i(\Delta t) = c_0 + \frac{2\gamma_e}{3k_s c_0}\int_{T_0}^{T_{e,i}(\Delta t)} C_{e,n}\,dT + \frac{2\gamma_l}{3k_s c_0}\int_{T_0}^{T_{l,i}(\Delta t)} C_{l,n}\,dT. \qquad (6)$$

Here, $C_{e,n}$ and $C_{l,n}$ are the electron and lattice heat capacities per atom and T_0 is the temperature of the sample before laser excitation. $T_{e,i}(\Delta t)$ and $T_{l,i}(\Delta t)$ are the average values of electronic and lattice temperatures of the ith and $(i + 1)$th layer at a delay time Δt after laser excitation. $\gamma_e = 1.4$ and $\gamma_l = 1.9$ (Ref. 48) denote the electronic and lattice Grueneisen constants, which are defined as the thermodynamic relation between the pressure increase, p, upon a change of the energy density, E/V, at constant volume, i.e., $\gamma_{e/l} = V(\partial p/\partial E_{e/l})_V$. However, we note that this thermodynamic relationship might not be always applicable on the ultrafast time scale and for non-equilibrium system.

We solve the equations of motion of the linear chain using a Verlet algorithm[49] and thus obtain the temporal change of the perpendicular unit cell dimensions at different depths z within the sample. By using $c(z, \Delta t)$ and $\Delta\langle u^2\rangle(z, \Delta t)$ as input for the dynamical diffraction simulation we can predict the temporal change of the diffraction pattern for comparison with the experimentally obtained pattern change.

IV. RESULTS AND DISCUSSION

A. Qualitative features in dynamical scattering from static crystal surfaces

In Fig. 2(a), we show the results of a dynamical scattering simulation for the specular diffraction spot of a Ni(100) surface. On the right-hand side of Fig. 2(a) the results for the reflectivity of the specular spot, i.e., the intensity of the specular spot, $I_{(00)}$, divided by the intensity of the incident beam, I_0, is plotted as a function of the incidence angle θ and the azimuthal angle ϕ relative to the [110] zone axis.

To verify the validity of the diffraction simulation we compare the experimentally observed ϕ-dependence of the specular spot intensity (for a given incidence angle $\theta = 5.3^\circ$) to the theoretically prediction, as shown in Fig. 2(b). Both, the positions and the intensity maxima are well reproduced.[50]

The qualitative features of the diffraction map (ϕ, θ) can be rationalized, as depicted on the left side of Fig. 2(a), by considering two distinct scattering mechanisms, namely direct Bragg (DB) scattering, a single scattering event qualitatively well described by kinematical scattering theory, and surface wave resonances (SWR), which are inherently multiple scattering events.

Direct Bragg scattering occurs when the incidence angle θ is close to a Bragg angle θ_B, defined through

$$\sqrt{(\sin\theta_B|k_0|)^2 + U} = \frac{nc^*}{2}, \qquad (7)$$

where c^* is the reciprocal unit cell vector perpendicular to the surface and n is an integer. U is related to the mean inner potential V by $U = eV2m/\hbar^2$ which leads to an acceleration of the electron beam when it enters the sample, equivalently to optical refraction. We note that for $U = 0$, the Bragg condition is recovered in its common form, i.e., $n\lambda = 2d\sin\theta_B$ with the electron beam wavelength λ and the crystallographic interplanar distance d.

The Bragg angles for different reciprocal lattice points $(00n)$ are indicated as blue lines in Fig. 2(a). It is important to notice that the intensity for direct Bragg scattering (into the specular direction) is independent of the azimuthal angle ϕ. Any intensity variation with ϕ, as seen in the numerical simulation (right part of Fig. 2(a)), has to be caused by multiple scattering events.

In surface wave resonances, the incidence beam is not directly scattered into an outgoing beam but couples with a beam parallel or almost parallel to the surface which in turn diffracts into the outgoing beam (see Fig. 2(c)). As it is shown in Appendix A, surface wave resonances can occur if the

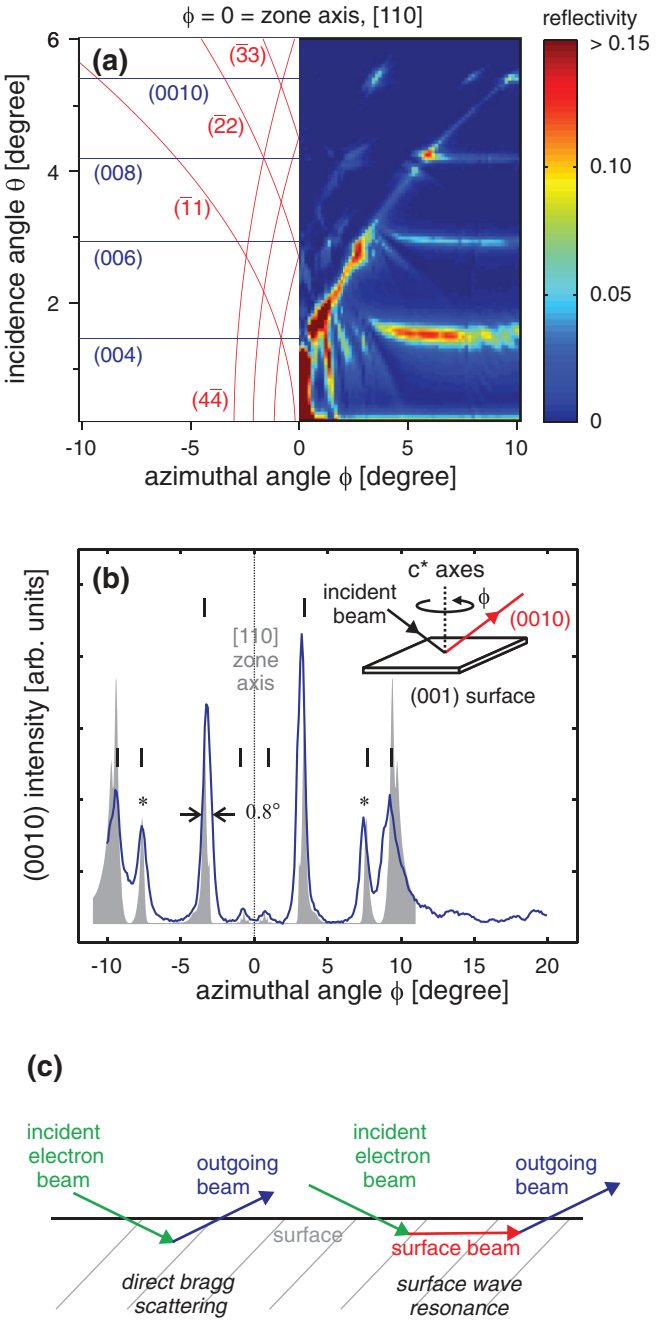

FIG. 2. Ni(100) diffraction map for the specular diffraction spot. (a) The calculated (ϕ, θ)-dependent reflectivity of the specular diffraction spot from a Ni(100) surface near the [110] azimuth is shown on the top right. The qualitative features of the map can be rationalized by considering the Bragg angles (blue lines) and surface wave resonance conditions (red lines) depicted on the top left (see text and Appendix A for details). (b) The ϕ-dependence of the calculated reflectivity (shaded gray area) is compared to the experimentally determined intensity (blue line) of the specular spot for a fixed incidence angle $\theta = 5.3°$, corresponding to the (0010) diffraction condition. ϕ-values that allow SWR according to Eq. (8) are indicated by vertical black lines. (c) Schematical comparison of the involved beams in a direct Bragg scattering and a surface wave resonance regime.

following relation between θ and ϕ is satisfied,

$$\phi = \frac{\xi}{2ha^*k_0} + \frac{\left(\xi - 2k_0^2\right)\theta^2}{2\sqrt{(2ha^*k_0)^2 - \xi^2}},$$
$$\text{with} \quad \xi = h^2a^{*2} + c^{*2}n^2. \tag{8}$$

The resulting parabolas are shown in the left-hand side of Fig. 2(a). Direct Bragg scattering together with surface wave resonances allow a clear interpretation of the numerical results shown on the left side of Fig. 2(a). At small θ and near the zone axis, the reflected intensity is strongly affected by multiple scattering events and the qualitative behavior can be well understood by considering surface wave resonance. No clear Bragg scattering is visible. At moderately small θ and sufficiently far away from the zone axis, a semi-kinematical regime can be observed. Surface wave resonances only play a minor role here and intensity maxima occur at the Bragg angles. And that is why some electron microscopy experiments are conducted away from the zone axis.[51] Only small variations of the intensity with changing ϕ are observed. Another regime can be recognized at high incidence angles. Here, intensity maxima occur if the conditions for surface wave resonances overlap with Bragg conditions, so that the reflectivity is, both, highly sensitive to the incidence and the azimuthal angle. This regime is often utilized in reflection electron microscopy[16] and in the monitoring of molecular beam epitaxy[52] since it offers a high sensitivity to structural changes while still providing a reasonable intensity of scattered electrons. Also in recent UEC experiments such a condition was adopted.[22,53]

With these different regimes and their underlying scattering mechanisms in mind we are now able to discuss how photo-excitation affects the diffraction map.

B. Temporal changes of the scattering intensity

We considered two types of structural dynamics, namely heating of the lattice which results in an increased mean-square displacement of the individual atoms from their equilibrium position, and expansion of the crystal lattice perpendicular to the surface. In Fig. 3, we show for three different azimuthal angles, how the rocking curve of the specular spot, i.e., the diffraction intensity depending on the incidence angle, changes when the temperature of the lattice is raised from $T = 300$ K to 600 K (red lines), and when the lattice is expanded by 10% (green lines) each compared to the equilibrium structure (blue lines). As a reference, we also give in Fig. 3(d) the rocking curves as predicted by kinematical scattering theory.

To qualitatively understand the changes in the rocking curves at different azimuthal angles it is important to note how direct Bragg scatterings and surface wave resonances are affected by the lattice expansion or heating.

According to the Bragg condition (Eq. (7), for small inner potential U) a relative change $\Delta c/c$ in the lattice constant c leads to a corresponding relative change $\Delta\theta/\theta = -\Delta c/c$. Thus, for an expanding lattice each Bragg angle decreases, as can be seen for the kinematical scattering simulation in Fig. 3(d), for low incidence angles in Fig. 3(b), and for intermediate angles in Fig. 3(c). SWR conditions, on the contrary do not depend on c (for $n = 0$, see Eq. (8)), and therefore stay constant when the lattice expands perpendicular to the surface. An example of this behavior is the intensity peak in Fig. 3(b) marked with an arrow, which by comparison with Fig. 2(a) is due to a $(1\bar{1})$ surface wave resonance and

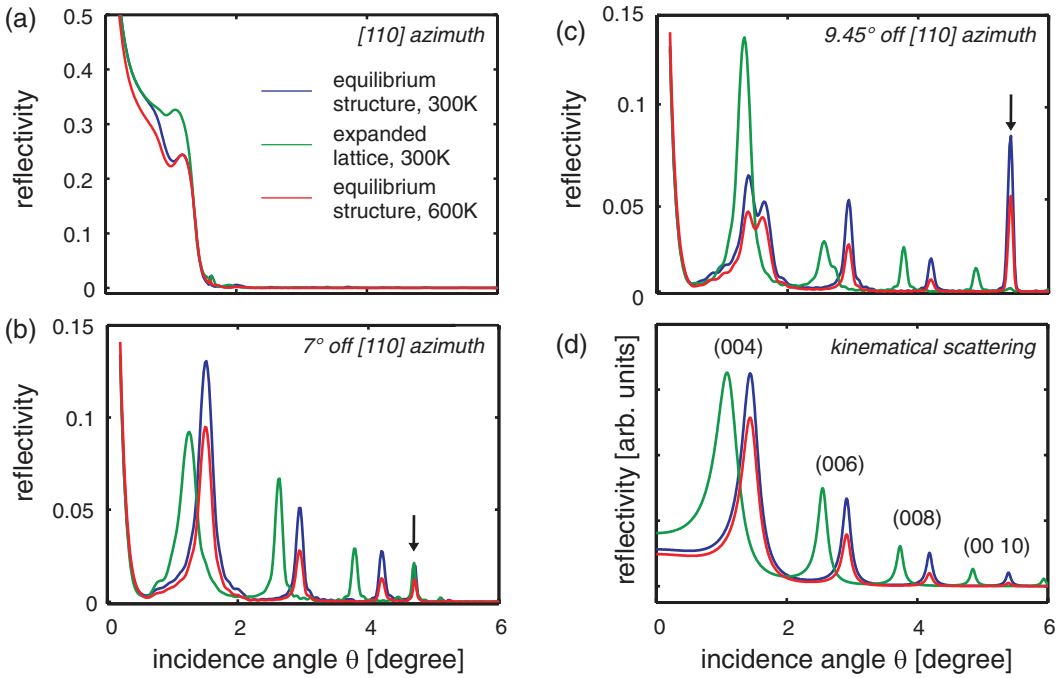

FIG. 3. Changes of the rocking curves upon heating and lattice expansion for different diffraction conditions. The rocking curves for a Ni(100) surface at equilibrium conditions ($T = 300$ K, equilibrium lattice constants, blue lines) are compared to the rocking curves for a lattice which is 10% expanded perpendicular to the surface (green lines), and a lattice at $T = 600$ K with the room temperature lattice constants (red lines). The azimuthal direction of the incident electron beam is either in the [110] zone axis (a), or 7° and 9.45° off the zone axis (b,c). As a reference, also the rocking curves in the kinematical scattering approximation are given in (d). The expected peak shift upon lattice expansion and intensity drop upon heating, according to the kinematic approximation, are not reproduced in (a) and at high incidence angles in (b) due to the prevalence of multiple scattering events in these diffraction conditions. However, if the azimuthal angle is off the zone axis and for intermediate values of the incidence angle a kinematic behavior can be qualitatively recovered as can be seen in (b).

is not moving after lattice expansion. The marked peak in Fig. 3(c), on the contrary, satisfies for the equilibrium structure both the Bragg condition and the condition for the $(1\bar{1})$ surface wave resonance. Consequently, after lattice expansion the peak splits into two parts, one that stays at the position of the SWR, and one that moves to smaller incidence angles according to the changed Bragg condition. Since the high original intensity of the peak is due to the overlap of the DB and the SWR condition, after lattice expansion both peaks show additionally a considerably reduced intensity.

Similarly, the increase of the atomic mean square displacement due to lattice heating has a different impact on direct Bragg scattering and surface wave resonances. Since direct Bragg scattering is generated by the interference of single scattering events, the temperature-dependence of the diffracted intensity can be well described by the Debye-Waller formula

$$\ln(I/I_0) = -\langle (q \cdot u)^2 \rangle, \tag{9}$$

where u is the atomic displacement vector and $q = k_0 - k''$ the difference between the incoming and outgoing electron wave vector. Surface wave resonances are generated by multiple scattering events, each having scattering vectors q different from $k_0 - k''$ which in principle can lead to a complex temperature-dependence. However, in the multiple scattering regime the Debye-Waller behavior is also often observed,[54,55] but with an effective $q = q_{\text{eff}}$ which is no longer directly related to $k_0 - k''$. Since the successive scattering events in surface wave resonances show a smaller scattering angle than direct Bragg scattering (see Fig. 2(c)), it is expected that for surface wave resonances $q_{\text{eff}} < q$.

These behaviors explain the various intensity changes upon heating which are seen in Fig. 3. On the one hand, the intensity change of the maxima in Fig. 3(b), which already behaves quasi-kinematically upon lattice expansion, also show a clear resemblance of the intensity decrease as predicted by kinematic scattering (Fig. 3(d)), both in magnitude of the relative change and in the scaling behavior with increasing θ and thus increasing q. On the other hand, the intensity maxima which are produced by surface wave resonances (the marked peaks in Figs. 3(b) and 3(c)) show a smaller intensity change compared to nearby DB scattering features.

The temperature-dependence of the SWR intensity is further illustrated in Fig. 4. In the top part of Fig. 4(a) the simulated reflectivity of the (00)-spot for a fixed incidence angle of $\theta = 5.4°$ is depicted for different azimuthal angles ϕ at $T = 300$ K (blue line) and $T = 600$ K (red line). This is compared to the temperature change as obtained from a simple Debye-Waller behavior (green line), according to Eq. (9). It can be clearly seen that the intensity change is consistently smaller than the Debye-Waller prediction but also largely depends on the azimuthal angle ϕ, although q is independent of ϕ. Interestingly, the intensity is smaller on the left shoulder of the resonance feature (closer to the zone axis) than on the right one which leads to an apparent shift of the diffraction features.

This behavior is compared to the experimental results shown in the bottom part of Fig. 4(a). The intensity of the (0010) spot was recorded at different azimuthal angles before

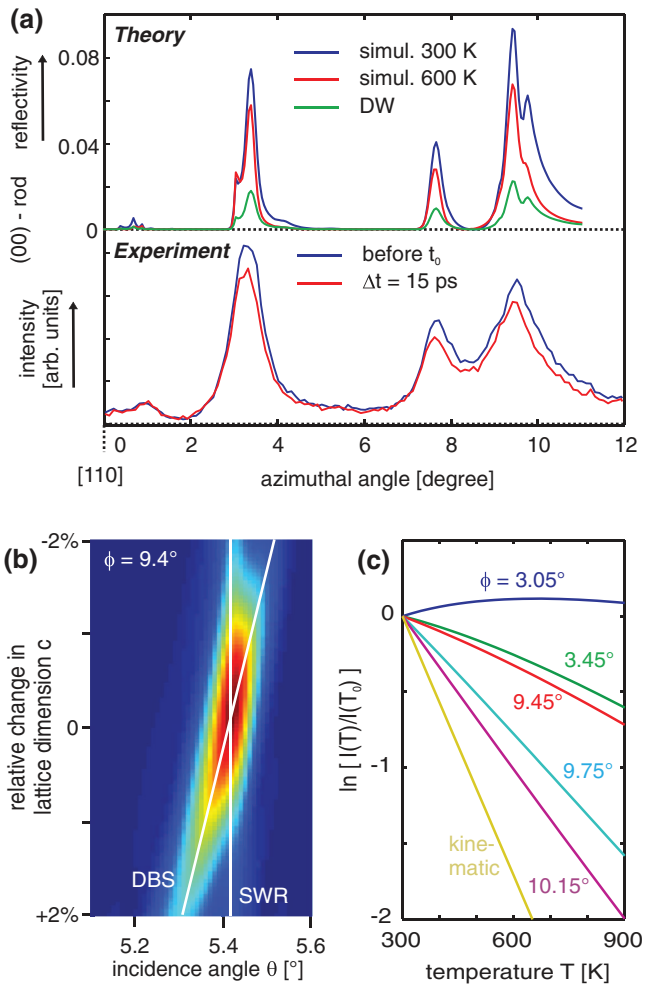

FIG. 4. Photo-induced intensity change of the (0010) Bragg spot for different azimuthal angles. (a) The simulated ϕ-dependence of the (0010) intensity for two different temperatures ($T = 300$ K (blue line); $T = 600$ K (red line)) is compared to the experimentally measured intensity before and 15 ps after laser excitation (estimated $T \approx 550$ K, see below). Both the shift of the SWR maxima towards the zone axis and the smaller intensity drop compared to kinematical scattering (green line) is reproduced in the experiment. (b) Change of the rocking curve at a SWR ($\phi = 9.4°$) upon a change of the lattice constant c. (c) The intensity drop of the (00 10) Bragg spot upon heating is compared for different azimuthal angles ϕ. The intensity drop in a SWR condition approximately follows a Debye-Waller-like behavior (Eq. (9)) with an effective q_{eff} which strongly depends on the azimuthal angle. The intensity increase at $\phi = 3.05°$ with raising temperature can be explained by multiple, competing scattering channels.

and 15 ps after laser excitation. As it is shown below, the laser excitation (13 mJ/cm^2) is expected to increase the temperature to ~550 K. Both the less pronounced intensity change after excitation, compared to the kinematical prediction, and the shift of the intensity maxima are reproduced in the experiment. The change in the rocking curve near the (0010) Bragg condition for different relative changes in the lattice parameter c is illustrated in Fig. 4(b) which shows the different behavior of the DBS and SWR upon lattice expansion. Figure 4(c) indicates that although the heating-induced intensity change strongly depends on the diffraction condition, for most conditions there is still, qualitatively, a Debye-Waller-like dependence on the temperature increase, i.e., $\ln(I/I_0) \propto \Delta T$.

In summary, for both the heating and expansion in the kinematic regime the structural dynamical features can be obtained. In the multiple-scattering regime, the observed changes in intensity or in expansion of the lattice become lower than those of the kinematic regime and thus provide the lower limit values characteristic of structural dynamics.

C. Connection between the diffraction map and the diffraction pattern

At this point it is important to keep in mind how UEC experiments are performed. In general, first without laser excitation, a specific diffraction condition is selected by changing the orientation of the sample relative to the electron beam. Then, diffraction patterns are recorded at a fixed sample orientation but with different temporal delays between the excitation laser and the probing electron beam. Therefore, we have to consider in which way the diffraction map and especially its changes due to laser-induced structural dynamics, as discussed above, determines the experimentally recorded diffraction pattern.

First, we consider an ideal case, where the incident electron beam has a single, well-defined wave vector k_0 and the sample is perfectly flat and periodic in directions parallel to the surface. The wave vectors k'' of the diffracted beams (hk) can be then obtained by the Ewald construction (Fig. 5). Due to energy conservation, the incident and outgoing wave vectors lie on a sphere in reciprocal space and, due to momentum conservation, the parallel component of the momentum difference $k_0 - k''$ is quantized to reciprocal lattice vectors B_i. In particular for the specular beam, i.e., $B_i = 0$, we see (Fig. 5(a)) that the outgoing angle θ'' of the diffracted beam is equal to

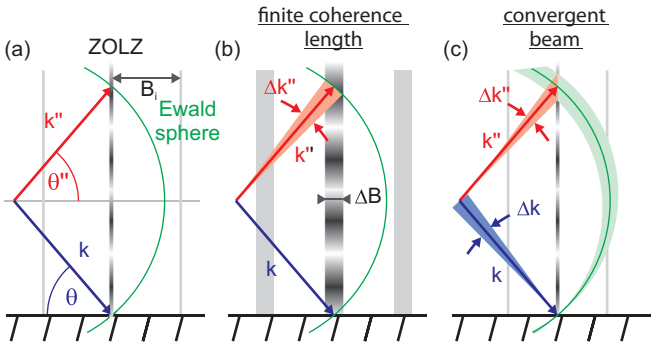

FIG. 5. Ewald construction for the specular spot. (a) Due to energy conservation, the incident and outgoing wave vectors k and k'' lie on a sphere in reciprocal space (green circle). The periodicity of the surface structure leads to a quantized momentum transfer parallel to the surface, with allowed valued according to reciprocal lattice rods B_i (gray lines). The wave vectors of observed diffracted beams lie at the intersection of the Ewald sphere with reciprocal lattice rods. For an idealized system with a well-defined incidence wave vector k and perfect periodicity parallel to the surface, the wave vector k'' of the diffracted specular beam is sharply defined with an outgoing angle θ'' equal to the incidence angle θ (independent of structural dynamics). (b) If the quantization condition of the parallel momentum transfer is partly relaxed by ΔB due to surface defects, the specular beam shows a relative spread of $\Delta k''/k = \theta'' = \Delta B/\theta k$ in the outgoing wave vectors. The intensity within this allowed range of outgoing angles depends on the modulation along the reciprocal lattice rod. (c) Similarly, an incident beam with a range Δk of wave vectors (convergent beam) gives a distribution of outgoing wave vectors with $\Delta k'' = \Delta k$.

the incidence angle θ. The outgoing angle, and thereby the position of the detected diffraction spot, does not depend on the actual lattice and therefore does not change due to structural dynamics.

However, in previous experiments diffraction spot movements were observed after laser excitation (see, e.g., Refs. 8 and 53). These results are understood provided the more realistic diffraction conditions shown in Figs. 5(b) and 5(c) are considered when the diffraction rods have a finite width due to a finite coherence length (Fig. 5(b)) or when the beam is made convergent (Fig. 5(c)).

A finite coherence length, due to, e.g., defects, breaks the periodicity parallel to the surface which partially relaxes the quantization of the parallel component of $k_0 - k''$. This leads to a broadening of the perpendicular rods in the Ewald construction (Fig. 5(b)) on the order of $\Delta B = 2\pi/\Delta l$, where Δl is the coherence length.[56] The Ewald sphere cuts the broadened rod at different heights which gives a distribution of outgoing angles around θ with a width $\Delta\theta'' \approx \Delta B/\theta k$. For typical values of $\theta = 5^\circ$ and $\Delta l = 20$ nm, one obtains $\Delta\theta'' = 0.2^\circ$. We note that the higher the incidence angle θ the smaller the window $\Delta\theta$ at a given coherence length Δl.

The intensity $I(\theta'')$ of the beams at different $\theta'' = \theta + \Delta\theta$ depends both on the modulation along the diffraction rod, as calculated from the dynamical scattering simulation, and on the modulation of the rod parallel to the surface. In a simple, semi-kinematic picture we assume that $I(\theta + \Delta\theta)$ can be written as $I(\theta + \Delta\theta) \propto I_{\mathrm{dyn}}(\theta + \Delta\theta) \times I_{\Delta l}(\Delta\theta)$, where $I_{\mathrm{dyn}}(\theta + \Delta\theta/2)$ is the intensity of a beam in the ideal case (see Fig. 5(a)) with an incidence angle of $\theta + \Delta\theta/2$. $I_{\Delta l}(\Delta\theta)$ depends in a complicated way on the coherence length.[56,57] For illustrative purposes we use a Lorentzian function for $I_{\Delta l}(\Delta\theta)$ (shaded area in Fig. 6). Overall, sample disorder causes the diffracted beam to contain information about the reflectivity not only at θ but in a certain region around θ, so that this part of the diffraction map is imaged onto the detector. This effect can be more directly obtained by using a finite beam convergence angle of the probing electrons, as depicted in Fig. 5(c). However, in the present experimental setup the beam convergence angle is smaller than 0.05° and can be neglected in most cases.

The imaging mechanism explains why in previous experiments a spot movement could be detected, since shifting diffraction features in the diffraction map then lead to a shift in the intensity distribution $I(\theta'')$ and therefore to a shift of the diffraction spot position. However, to quantitatively relate the shift of the diffraction spot with the change in the diffraction map it is important to consider the width of the sampled θ-region (due to the finite coherence length) compared to the width a diffraction feature in the diffraction map, as it is shown in Fig. 6. If the sampled θ-region is large or comparable to the width of the diffraction feature (Fig. 6, upper panels), the change in the diffraction map leads to an equal change in the spot position. However, for small sampled θ-regions (Fig. 6, lower panels) we recover the behavior of the ideal diffraction case with no diffraction spot movement upon excitation (Fig. 5(a)). Since the sampled θ-region depends on the quality of the sample, which determines the width of the reciprocal lattice rods, different samples can give rise to different diffraction spot movements despite equal structural dynamics. The observed Bragg spot movement is only a lower limit of the amount of movement in the diffraction map.

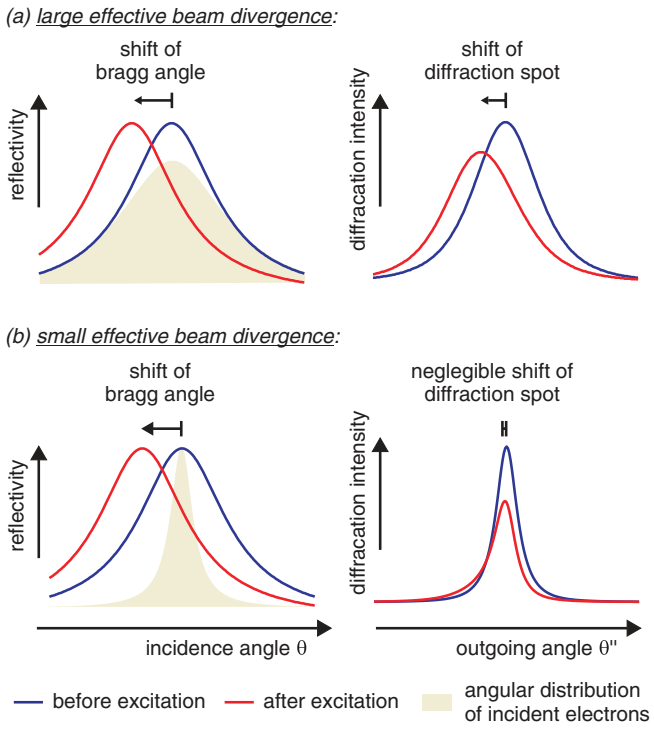

FIG. 6. Connection between the diffraction map and the diffraction pattern. In the left two panels the schematic shift of the Bragg condition before (blue) and after excitation (red) is shown. The shaded area signifies the effective divergence angle of the electron beam. The effective divergence angle is larger in the top panel compared to the bottom panel. The center of the distribution can be adjusted by tilting the sample whereas the width is, in the present setup, dominated by the sample quality (see Fig. 5(b) and discussion in the text). The right panels show the resulting change of the Bragg spot in the diffraction pattern. In the case of a large effective divergence (top panels) the shift in the Bragg spot qualitatively matches the shift in the diffraction map. For a small effective beam divergence, the Bragg spot is almost not moving after excitation (corresponding to Fig. 5(a)), but the Bragg spot intensity decreases significantly since the Bragg condition changes due to an expanding lattice.

This is shown in Fig. 7 using single crystalline graphite as an example. In the experimental rocking curve depicted in Fig. 7(a) (blue line) two intensity maxima of the specular (0014) spot are visible which correspond to two different graphite grains that are inclined to each other by $\sim 0.25^\circ$. After laser excitation (30 ps after time zero) both maxima shift by $\Delta\theta_B = 0.015^\circ$ to smaller incidence angles due to a thermal lattice expansion. At the same time the intensity drops are equal for both maxima, indicating an equal heating of both grains. This has to be contrasted to the shift of the diffraction spot position shown in Fig. 7(b). Whereas the diffraction spot generated by the first grain, which fulfills the Bragg condition for small incidence angles, shows a shift in the scattering angle $\theta + \theta'' \approx 2\theta_B$, as expected, the diffraction spot generated by the second grain shows a diminished deflection. This behavior can be rationalized by referring to Fig. 6. The broader first peak in Fig. 7(a) corresponds to the experimental case shown in upper two panels of Fig. 6, where the shift in the Bragg condition is reflected in a shift of the diffraction

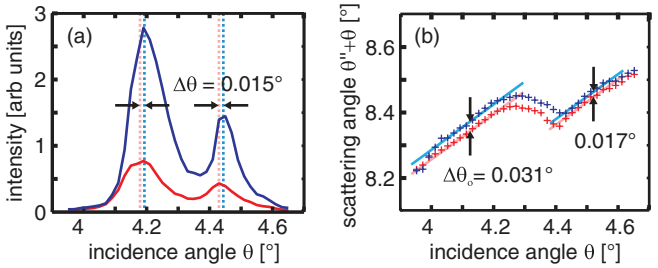

FIG. 7. Time-dependent rocking curve diffraction spot movement. (a) The experimental rocking curve of single crystalline graphite [near (0014) Bragg angle, $(2\bar{2})$ SWR] before (blue curve) and after excitation (red curve) is depicted. The two peaks in the rocking curve correspond to two single crystalline grains with a slight relative inclination of ~0.25°. The rocking curve after excitation shows an overall decreased intensity due to an increased atomic mean-square displacement and a uniform shift of 0.015° in the peak maxima indicating a lattice expansion of 0.36%. (b) The right panel shows the corresponding position of the (0014) Bragg spot (quantified by the scattering angle $\theta'' + \theta$) before (blue crosses) and after excitation (red crosses). As expected, the scattering angle of the Bragg spot decreases after excitation lattice expansion. However, contrary to the uniform shift of the rocking curve in (a), the two grains show a different spot movement. This can be explained by the different peak widths in the rocking curve of the grains together with the imaging mechanism shown in Fig. 6.

spot. The more narrow second peak in Fig. 7(a) corresponds to the situation depicted in the lower panels of Fig. 6, where the same shift in the Bragg condition leads only to a reduced shift in the diffraction spot.

D. Dynamical scattering in nickel and graphite

Having discussed the general phenomena which have to be taken into account for a quantitative interpretation of UEC experiments, we now wish to focus on two specific examples, namely the photo-induced dynamics of a nickel (100) surface and of a graphite (0001) surface.

In Fig. 8, the wave function components (see Eq. (2)) of the diffracted electron wave in a SWR condition (blue curves: specular/incident beam wave component $c_{(00)}$; red curves: surface wave component) and in a quasi-kinematic condition (green curves: specular/incident beam wave component $c_{(00)}$) are shown, both, for nickel (left panel) and graphite (right panel). Within a SWR the surface wave component gains a significant amplitude within the first few atomic layers and the specular/incident beam component decays accordingly. This, again, demonstrates that the fundamental assumption of kinematic scattering theory, that the scattered wave has a negligible amplitude compared to the incident wave, is inadequate for these cases. It can be seen that due to the higher scattering potential (see insets in Fig. 8) of nickel the incoming electron wave decays faster within the solid compared to graphite, although the qualitative picture remains the same.

In the following we will first compare the experimentally observed dynamics of the (0010) Bragg spot of a Ni(100) surface with the theoretical prediction using the dynamical scattering model outlined above and assuming the validity of the two-temperature model. In the last part we will discuss, what additional effects emerge for graphite due to its strong anisotropy and the larger penetration depth of the scattering electron, compared to the situation in nickel (Fig. 8).

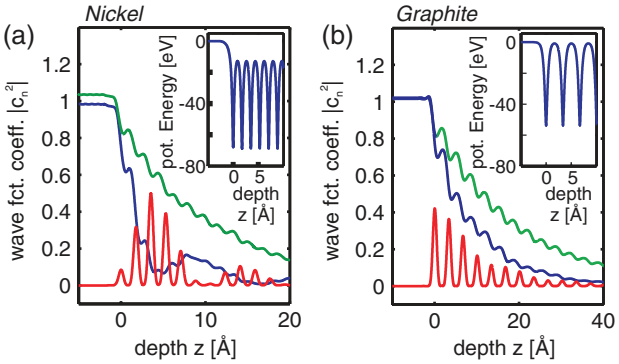

FIG. 8. Wave function of the diffracted electron for nickel (a) and graphite (b) depending on the depth z within the sample. (a) The wave function coefficients $|c_i|^2$ (Eq. (2)) for $B_i = (00)$ (green and blue lines) are calculated for an incidence angle $\theta = 5.4°$ ((0010) Bragg spot) and azimuthal angles of $\phi = 3.5°$ (blue line), corresponding to a $(2\bar{2})$ resonance, and $\phi = 12°$ (green line). The red line shows the depth-dependence of the surface beam $c_{(2\bar{2})}$ for $\phi = 3.5°$. It can be seen that within the SWR the wave function is localized within 1 nm with a substantial transfer of population from the incident $c_{(00)}$ beam to the tangential $c_{(2\bar{2})}$ beam. Outside of a SWR (green line) the wave function coefficient $c_{(00)}$ decays slower within the solid and the $c_{(2\bar{2})}$ coefficient gains no significant amplitude (not shown). The inset shows the average scattering potential depending on the depth z inside the sample. (b) In the same way, $c_{(00)}$ was calculated for graphite using $\theta = 3.995°$ ((0014) Bragg spot) and azimuthal angles of $\phi = 1.275°$ (relative to [110] zone axis, $(1\bar{1})$ SWR) and $\phi = 7°$ (no SWR). The qualitative picture is similar to (a) although, due to the smaller scattering potential (see inset), the length scale over which the wave function decays is stretched.

1. Dynamics of a clean Ni(100) surface

In Fig. 9(a), the dynamics of the electron and lattice temperature at the surface after excitation are shown for the used experimental fluences and simulated within the TTM. Because the penetration depth of the excitation laser (14 nm) is an order of magnitude larger than the penetration depth of the electron beam (1–2 nm), a homogeneously excited sample is effectively probed by the diffracted electron beam. Nevertheless, the inhomogeneous temperature distribution within the sample governs the time constant for the cooling dynamics and must be therefore retained in the model (spatial part of Eq. (3)).

The electron temperature at the surface rises according to the pulse width of the excitation laser and decays due to the electron heat conductivity and the energy transfer to the lattice temperature bath (electron-phonon coupling). The latter process also gives rise to the increase in the lattice temperature, which affects the diffraction intensity via the Debye-Waller effect.

The fluence dependence of the lattice temperature rise time can be understood by considering a simplified TTM without thermal conduction ($\kappa_e = 0$) using temperature-independent material constants. In this case, the lattice temperature shows an exponential rise with a time constant $\tau \approx C_e/g$. However, for a free electron gas C_e is not temperature independent but depends linearly on the temperature, whereas g is temperature independent. This leads to an increase of τ with the increase of fluence. Although for nickel the material constants show a significant deviation from the free electron gas,[39,40] which is also considered in our simulation, this qualitative trend is still retained.

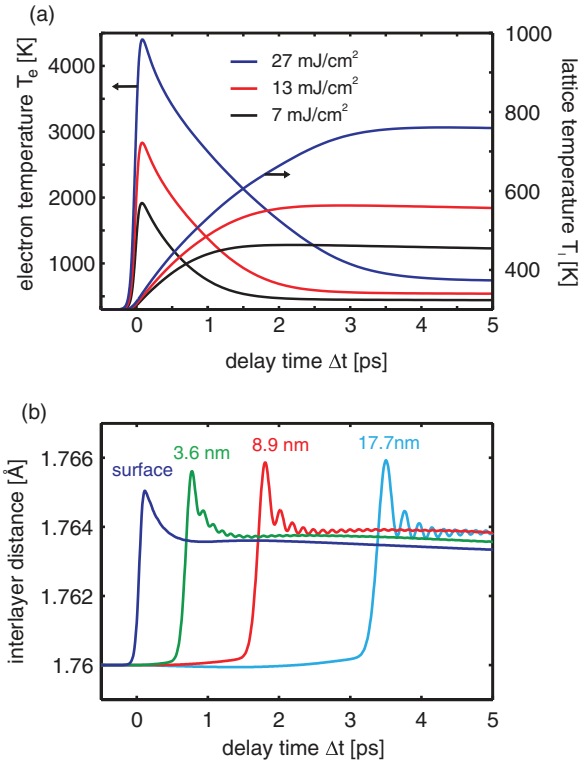

FIG. 9. Simulated heating dynamics of a Ni(100) surface (see text for details). (a) Temporal change of the electron (T_e) and lattice temperature (T_l) at the surface depending on the excitation fluence as predicted from a two-temperature model with temperature-dependent material constants. (b) The temporal change of the lattice constant for an excitation fluence of 7 mJ/cm^2 at different depths as obtained by combining the two-temperature model with a one-dimensional spring model.

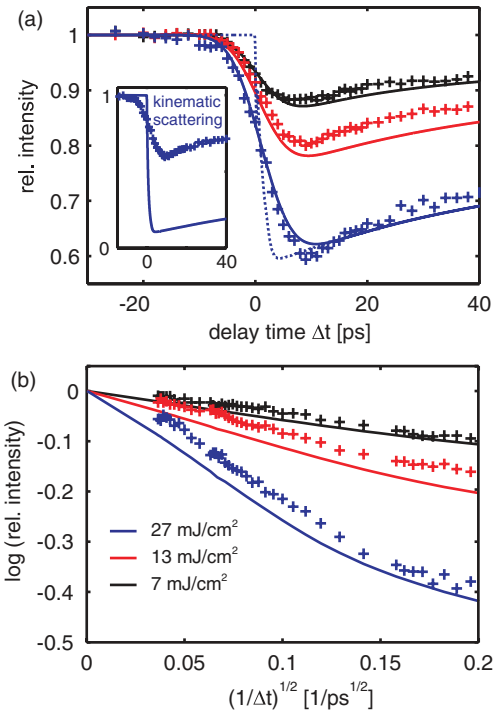

FIG. 10. Two-temperature model and Bragg peak intensity change. Comparison between the experimentally observed and theoretically predicted temporal drop of the (0010) Bragg spot intensity of a Ni(100) surface at an azimuthal angle of $\phi = 3.4°$. (a) The theoretically predicted heating dynamics (dotted line) are obtained by using the temporal change of the structure as deduced from a TTM (Fig. 9) and calculate the scattered intensity within dynamical scattering theory. To account for the finite temporal resolution the theoretical predicted drop is convoluted with a Gaussian (4 ps standard deviation). It has to be noted that the experimental data are quantitatively reproduced for different fluence by only using the known material constants of nickel. On the contrary, a kinematical scattering model severely overestimates the intensity drop due to lattice heating, as shown in the inset. (b) In a similar manner the cooling dynamics of the surface at longer times is well described, following a typical $1/\sqrt{t}$ behavior.

The temporal change of the electron and lattice temperature, and with this the change of the atomic mean-square displacement, additionally initiates a change of the lattice constant normal to the surface, i.e., Δc in the case of nickel. Using the known electronic and lattice Grueneisen constants and elastic properties of nickel (see Sec. III B), we obtain the temporal change of the lattice constant at different depths within the sample, as depicted in Fig. 9(b).

The distance between the topmost and second topmost layer (dark blue curve) shows the fastest response (limited by the half period of the interlayer vibration, here $T/2 \approx 105$ fs) with a fast component due to the initially hot electron system and a long time component mainly due to the increased lattice temperature.

Layers deeper within the sample can only expand when those on top of them have already expanded, so that their response is limited by z/v (z: depth within the sample, $v = 5277$ m/s the longitudinal sound velocity[37]). Taking the probing depth of the electron beam of 1–2 nm, we expect a time constant of the change in the Bragg spot of $\tau \approx 190-380$ fs (see Fig 11).

This is an interesting difference when compared to ultrafast transmission electron experiments. There, a thin metal film of thickness d is probed, which limits the change in the Bragg spot position (due to unit cell changes) to d/v.[58] For typical values of $d = 20$ nm and $v \approx 5000$ m/s, we obtain a temporal resolution limit in the dynamics of the unit cell dimensions of 4 ps. The interesting electronic contribution to the lattice expansion occurring at early delay time is therefore only indirectly accessible in a transmission scattering setup,[6,48] whereas the reflection setup, in principle, should allow their direct observation.

Taking the predicted temporal dynamics of the mean-square displacement and the unit cell changes, we construct a dynamical structure model of the surface and calculate the subsequent temporal changes of the diffraction pattern within the dynamical diffraction model.

In Fig. 10(a), we compare the calculated change in the intensity of the (0010) Bragg spot (solid lines) for different fluences F to the experimentally observed intensity change. To account for the experimental time-resolution, the theoretically predicted dynamics was convoluted with a Gaussian (4 ps standard deviation in this case). As an example, the unconvoluted intensity dynamics for $F = 27$ mJ/cm^2 is shown as a dotted line. We putatively attribute the limited time-resolution in this study to the large electron footprint ($\sim$2 mm) on the sample within the grazing incidence configuration, although the largest part of the thereby generated velocity mismatch between electron pulse and laser pulse is expected to be compensated by the tilted excitation scheme.[20]

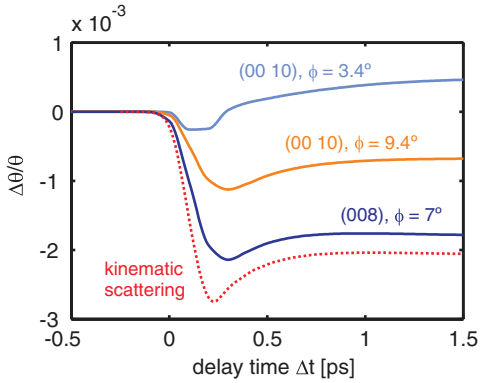

FIG. 11. Simulated dynamics of the relative Bragg angle change. Within kinematic scattering theory (dotted red line) the relative change $\Delta\theta/\theta$ of the Bragg angle of a specular spot (due to lattice expansion) is independent of the order of the spot. Within dynamical scattering theory (solid lines) the relative shift of the Bragg spot depends on the azimuthal orientation ϕ and the incidence angle θ. A reduced shift is observed in a SWR (light blue and red line). In an off-resonance condition the shift predicted by dynamical scattering is close to the kinematical results (dark blue line).

Preliminary results using smaller sample sizes gave an increased time-resolution (~2 ps) and experiments using an improved electron gun design with decreased spot size are currently being performed. It is important to note that the good agreement between theoretically predicted intensity change and experimental results is achieved without any adjustable parameters and only by using the known material constants of nickel. Furthermore, including dynamical scattering effects is crucial. As it is shown in the inset, a kinematic scattering model would severely underestimate the intensity change by a factor of two (the mean-square displacement increases logarithmically).

The cooling dynamics shown for long delay times in the lower panel of Fig. 10 can be also reasonably well described using Eq. (5), provided that the reduced intensity change due to dynamical scattering is taken into account.

In Fig. 11, we show the predicted relative shifts of the Bragg angles, $\Delta\theta/\theta$, for the specular spot at different delay times Δt using the results of the TTM together with the one-dimensional spring model as input to the dynamical scattering calculation. The shift within kinematical scattering theory (dotted red line) closely resembles the predicted change in the interlayer distance Δc near the surface as shown in Fig. 9, since $\Delta\theta/\theta \approx \Delta c/c$. Furthermore, $\Delta\theta/\theta$ is independent of the incidence angle θ (order of the Bragg spot), or the azimuthal orientation ϕ. However, within dynamical scattering theory $\Delta\theta/\theta$, shown in Fig. 11 (solid lines), depends both on the incidence angle and the azimuthal orientation. Especially in a SWR condition (light blue and red line) the movement of the Bragg spot is significantly reduced since the resonance condition does not change with an expanding lattice, as already discussed above in relation to Fig. 4(b). Experimentally, we do not observe any time-dependent shift in the position of the (0010) Bragg spot (within an experimental uncertainty of $|\Delta\theta/\theta| < 0.0005$) in agreement with the theoretical prediction for $\phi = 3.4°$ (light blue curve).

2. Dynamics of single crystalline graphite

For the second example we discuss the implications of dynamical scattering effects on the measured structural dynamics of graphite. Graphite differs in two respects from the previous example of Ni(100). First, graphite is a layered material and shows a strong anisotropy for the properties parallel and perpendicular to the layers. Within kinematic theory only motions parallel to the scattering vector are probed in a diffraction setup. By choosing an adequate diffraction condition either motions within the layers or in a perpendicular direction can be selectively studied. However, in dynamical scattering theory a set of electron waves with different directions and hence different scattering vectors are simultaneously excited, so that atomic motions in different directions are probed.

Second, due to the low atomic number and atomic density the penetration depth of the probing electron is larger in graphite than in nickel (see Fig. 8), which leads to sharper peaks in the rocking curve, so that peak shifts will have also an effect on the observed scattered intensity at a fixed incidence angle θ, as discussed in Sec. IV C.

To discuss the relative significance of these two features on the observed transient diffraction pattern, we employ a simplified model for the structural dynamics of graphite. The actual structural dynamics in graphite involves more than lattice heating as discussed in Ref. 59. In our simplified model, we assume that the in-plane atomic motions couple to the electronic degrees of freedom with a time constant of $\tau_1 = 2$ ps. The out-of-plane motions subsequently equilibrate with the in-plane motions on a time scale of 7 ps leading to a temporal change of the in-plane temperature, $T_\parallel$, and the out-of-plane temperature, $T_\perp$, as depicted in Fig. 12.

The effect of $T_\parallel \neq T_\perp$ on the Bragg peak intensity of the specular spot in a SWR condition is shown in Fig. 13(a) by calculating the intensity of the (0014) Bragg spot at different temperatures $T_\perp = T$ (red curve) or $T_\parallel = T$ (green curve), while keeping the temperature for movements in the other direction constant. For comparison, also the temperature-dependent intensity for an equilibrated lattice (blue curve) is depicted together with the kinematically predicted Debye-Waller behavior (pink curve) and the intensity change within a semi-kinematical scattering condition (light blue curve, out

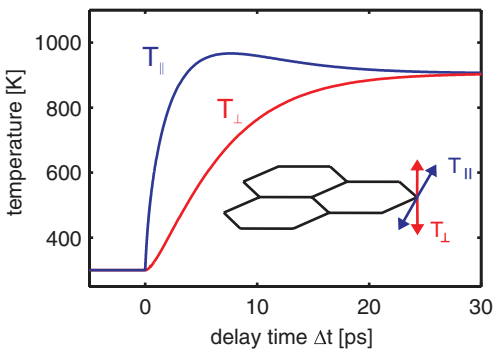

FIG. 12. Simulated heating dynamics of the in-plane and out-of-plane vibrational modes in graphite at an excitation fluence of 10 mJ/cm^2. The material constants were taken from Refs. 60–62.

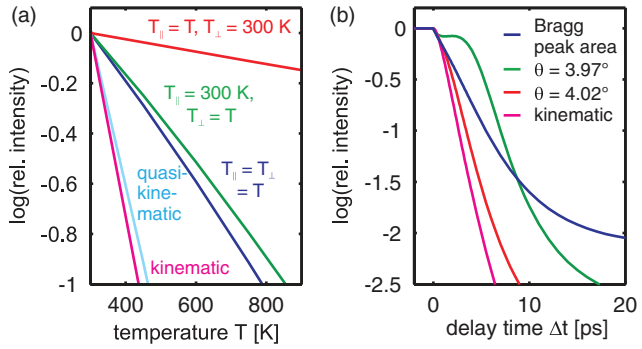

FIG. 13. Influence of dynamical scattering on the observed photo-induced diffraction pattern changes in graphite. (a) Intensity of the (0014) Bragg spot at the $(1\bar{1})$-SWR for different temperatures T. The blue curve shows the intensity drop when the in-plane and out-of-plane vibrations are in thermal equilibrium with each other at a temperature T. The red (green) curve refer to non-equilibrium scenarios where the in-plane (out-of-plane) vibrations are at a temperature T and the out-of-plane (in-plane) vibrations are at a temperature of 300 K. For comparison, also the kinematically predicted intensity drop is shown (pink line) together with the calculated intensity drop for an azimuthal angle of $\phi = 7^\circ$ (no SWR, light blue line). This shows that the reduced intensity drop upon heating in a SWR as discussed for nickel is also observed in graphite. Furthermore, due to the coupling of the incident electron beam to a tangential surface beam the intensity drop is not only dependent on the out-of-plane vibrational temperature but also on the in-plane temperature. (b) Simulated temporal intensity drop of the (0014) Bragg spot using the time-dependent temperatures shown in Fig. 12 showing the difference in the relative, temporal change of the Bragg area in the rocking curve (blue line), the relative change in the reflectivity for incidence angles of $\theta = 3.97^\circ$ (green line) and $\theta = 4.02^\circ$ (red line), and the intensity dynamics as predicted by kinematical scattering (pink line). The different behaviors can be explained by the interplay between lattice expansion and lattice heating and their effect on the rocking curve as displayed in Fig. 14.

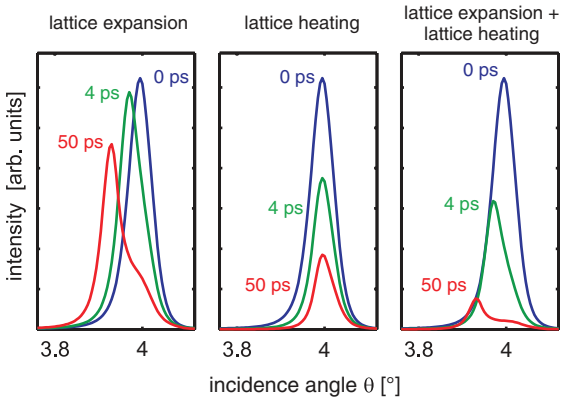

FIG. 14. Influence of lattice expansion and lattice heating on time-dependent rocking curves for the (0014) Bragg spot in graphite. Rocking curves at delay times $\Delta t = -5$ ps, 4 ps, and 50 ps using either only the predicted lattice expansion (left panel), only the lattice heating (middle panel) or both, lattice expansion and lattice heating.

of SWR). Within kinematical scattering the intensity of the (0014) Bragg spot only depends on the out-of-plane temperature, $T_\perp$. When a SWR condition is chosen, not only the effective Debye-Waller is decreased, as already observed for Ni(100), but also the diffracted intensity depends on both the in-plane and out-of-plane temperature. However, for the case of graphite with the in-plane Debye temperature $\theta_{D,\parallel} = 1300$ K, which is significantly larger than the out-of-plane one, $\theta_{D,\perp} = 530$ K,[61] the in-plane movements only give a small contribution (~15%) to the intensity decrease of the (0014) Bragg spot.

To assess the effect of temporal changes in the rocking curve on the observed dynamics of the (0014) Bragg spot, we use the predicted temporal behavior of the temperatures $T_\parallel$ and $T_\perp$ (Fig. 12) and simulate the Bragg spot intensity at different incident angles (Fig. 13(b)) and the rocking curves (Fig. 14) for different delay times Δt assuming a thermal expansion of the lattice. In the left panel of Fig. 14 only the expansion of the lattice (without heating) is considered in the simulation of the rocking curve, whereas in the middle panel the lattice heating (without expansion) is taken into account. The right panel shows the temporal change of the (0014) rocking curve for the physically relevant case of both lattice heating and expansion.

As expected, lattice expansion alone leads to a time-dependent shift in the peak of the rocking curve, although additionally a decrease in diffracted intensity and a change in the rocking curve shape is apparent (see also Fig. 4(b)). Lattice heating (without expansion) leads to a Debye-Waller-like effect with a decreased effective Debye-Waller factor as already discussed above. Combined lattice heating and expansion (Fig. 14, right panel) gives a time-dependent change of the position and shape of the rocking-curve maximum, mainly produced by the lattice expansion, and a decrease in the maximum intensity produced by both the lattice expansion and the lattice heating. With this temporal change of the rocking curve the time-dependent change of the diffracted intensity at different incidence angles (Fig. 13(b)), i.e., positions in the rocking curve can be rationalized. If the incident angle is chosen at the maximum of the rocking curve before excitation, $\theta = 4.02^\circ$, a fast decrease of the diffracted intensity is observed (Fig. 13(b), red curve) due to both lattice expansion and lattice heating. However, if the incidence angle is chosen to be slightly smaller, $\theta = 3.97^\circ$, the intensity in the first ~5 ps stays almost constant, since the decrease of diffracted intensity due to the Debye-Waller effect is compensated by the lattice expansion which shifts the maximum of the rocking curve closer to $\theta = 3.97^\circ$. At later times the lattice expansion leads to rocking curve maxima smaller than 3.97°, so that the diffracted intensity now shows a marked decrease.

It is important to note from the observed intensity change for $\theta = 3.97^\circ$ and $\theta = 4.02^\circ$ that for the case of graphite it is necessary to observe the change of the total rocking curve after excitation in order to obtain quantitative information about the underlying dynamics.

V. CONCLUSION

In this contribution, we have studied experimentally two samples such as nickel and graphite using UEC under ultrahigh vacuum conditions. Comparison with theory in the kinematical and dynamical scattering regimes have been examined highlighting the importance of obtaining "diffraction maps" which we define by both the Bragg angle θ and the azimuthal angle ϕ. It is shown that multiple scattering effects are important and can be rationalized. Their most significant influence is in showing that kinematical analysis underestimates the values of lattice temperature (mean-square

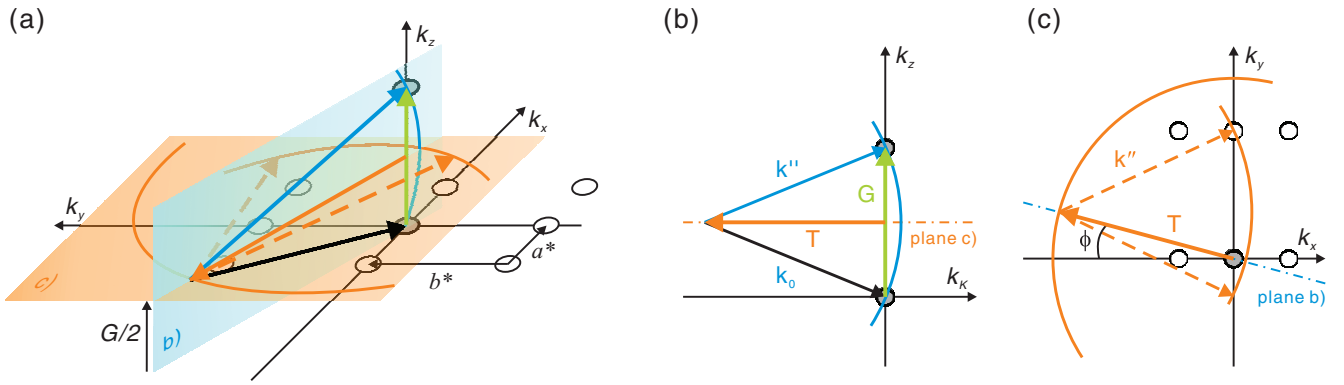

FIG. 15. Geometrical construction of the surface wave resonance condition (see text for details). (b and c) Two-dimensional cuts of the Ewald construction depicted in (a).

displacement) and lattice expansion, thus the observed values represent lower limits of dynamical changes. Finally, we examined the effect of lattice anisotropy (graphite), penetration depth, finite coherence length and order of diffraction on the observed Bragg peaks shift and hence structural expansion. We expect that the reported results will enhance the level of applications for future ultrafast electron diffraction studies.

ACKNOWLEDGMENTS

This work was supported by the National Science Foundation (NSF) and the Air Force Office of Scientific Research (USAFOSR) in the Center for Physical Biology at Caltech supported by the Gordon and Betty Moore Foundation. One of the authors (S.S.) gratefully acknowledges a scholarship from the Alexander von Humboldt-Foundation.

APPENDIX A: SURFACE WAVE RESONANCES

A surface wave resonance occurs when the incoming electron beam can diffract into a beam running parallel or almost parallel to the surface as well as into an outgoing electron beam. Thus, unlike the kinematical scattering picture, there are at least three beams involved in the scattering process. Using a geometrical construction (Fig. 15), we wish to derive in which azimuthal orientation of the sample a surface wave resonance can exist. The incident electron beam has a wave vector $\boldsymbol{k}_0$ (black arrow, Figs. 15(a) and 15(b)) and is elastically diffracted into an outgoing beam with a wave vector $\boldsymbol{k}'' = \boldsymbol{k}_0 + \boldsymbol{G}$ (blue arrow), where G is a reciprocal lattice vector normal to the surface. Since the scattering process is elastic both the incident and scattered wave vectors have the same length, $|\boldsymbol{k}_0| = |\boldsymbol{k}_0 + \boldsymbol{G}|$, and therefore the endpoints of the wave vectors lie on a sphere (Ewald sphere) with its center at $\boldsymbol{T}$:

$$T = \begin{pmatrix} \sqrt{\boldsymbol{k}_0^2 - (\boldsymbol{G}/2)^2}\,\sin\phi \\ \sqrt{\boldsymbol{k}_0^2 - (\boldsymbol{G}/2)^2}\,\cos\phi \\ |\boldsymbol{G}|/2 \end{pmatrix}. \tag{A1}$$

In this situation a surface wave can be excited (broken, orange arrow in Figs. 15(a) and 15(c)), if the Ewald sphere cuts an additional reciprocal lattice rod at a point $\boldsymbol{G}'$ with $G'_z = |\boldsymbol{G}|/2 + \Delta G'$. The x- and y-component of $\boldsymbol{G}'$ are restricted to multiples of the unit mesh of the reciprocal surface net, i.e., $G'_x = ha^*$ and $G'_y = kb^*$. In the following we restrict the derivation to $G'_y = 0$ although the more general case can be easily incorporated. For a beam parallel to the surface, $\Delta G'$ is equal to zero. Experimentally, (weaker) resonances with $\Delta G' = c^*n$ (c^* reciprocal lattice vector normal to the surface) are observed, where n is a small integer. In these cases the surface beam has a small angle relative to the surface.

In order for $\boldsymbol{G}'$ to lie on the Ewald sphere, $|\boldsymbol{G}' - \boldsymbol{T}| = |\boldsymbol{k}_0|$ must hold. Using the Bragg equation, $|\boldsymbol{G}|/2 = \sin\theta$, and considering small angles θ, gives the following relation between the incidence angle θ and the azimuthal angle ϕ, for which a SWR can be formed,

$$\phi = \frac{\xi}{2ha^*|\boldsymbol{k}_0|} + \frac{\left(\xi - 2\boldsymbol{k}_0^2\right)\theta^2}{2\sqrt{(2ha^*|\boldsymbol{k}_0|)^2 - \xi^2}}, \tag{A2}$$

where

$$\xi = h^2a^{*2} + c^{*2}n^2. \tag{A3}$$

Furthermore, the influence of the potential step V at the surface can be included, by defining ξ as $\xi = a^{*2} + c^{*2}n^2 - V$. Thus, in the diffraction map SWR conditions are satisfied along parabolic curves. For the strongest resonances with $n = 0$ ($\Delta G' = 0$), the parabola only depend on the reciprocal lattice dimensions parallel to the surface and the potential step at the surface. Therefore, the SWR parabola do not change upon lattice expansion.

APPENDIX B: SAMPLE PREPARATION AND CHARACTERIZATION

The Ni(100) surface was prepared from a nickel single crystal (Accumet Materials Co., 4N5 purity, $< 0.5^\circ$ miscut) by repeated sputtering (300 eV, Ar^+) and annealing ($\sim$900 K) cycles as reported in the literature.[63] Prior to transferring the sample to the UEC chamber, the final cleanliness

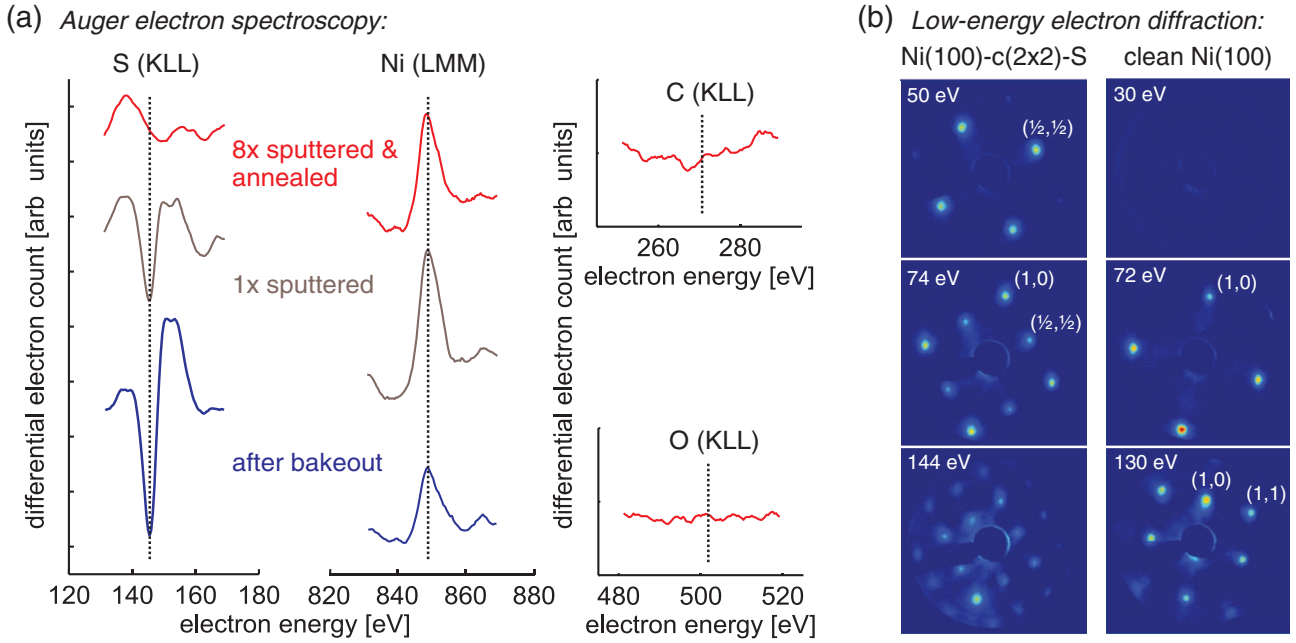

FIG. 16. Sample characterization (a) Auger electron spectra of the Ni(100) sample at the S(KLL), Ni(LMM), C(KLL), and O(KLL) transition energies. (b) LEED pattern of the nickel without cleaning steps (showing a Ni(100)-c(2×2)-S adsorbate structure) and the diffraction pattern of the sample after several sputtering and annealing cycles.

of the surface was verified by low-energy electron diffraction (LEED) and Auger electron spectroscopy. In Fig. 16(a) (left and middle panels) the Auger electron spectra near the sulfur (KLL)-transition and the nickel (LMM)-transition are shown for the nickel sample prior to cleaning, after one ion-sputtering step and after eight sputtering/annealing cycles. Prior to cleaning, the surface was contaminated by sulfur, which was removed by the sputtering/annealing cycles leading to a vanishing sulfur signal[64] and an increased nickel signal in the Auger electron spectrum. Also carbon and oxygen impurities Fig. 16(a) (right panels) can be ruled out for the cleaned surface. The low-energy diffraction pattern Fig. 16(b) for the uncleaned (left panel) and cleaned surface (right panel) show both well-defined diffraction spots with a low background intensity, indicating ordered surfaces. The surface structure before cleaning is attributed to nickel surface with an ordered sulfur over-layer, i.e., Ni(100)-c(2×2)-S. The half-order diffraction spots disappear after sputtering and only the spots that originating from a Ni(100) remain.

The base pressure in the apparatus is in the lower 10^{-10} Torr range. Since the time-resolved diffraction patterns are recorded over a few days, it is expected that during this period the surface gets again contaminated to some degree. However, we did not observe any deterioration of the RHEED pattern in the course of the experiment. Heavy surface contamination, as observed on a nickel single crystal without the above described cleaning steps, on the contrary, led to drastically reduced Bragg spot intensities with diffuse spot profiles.

[1]A. H. Zewail and J. M. Thomas, *4D Electron Microscopy: Imaging in Space and Time* (Imperial College Press, London, 2010), and references therein.
[2]R. J. D. Miller, R. Ernstorfer, M. Harb, M. Gao, C. T. Hebeisen, H. Jean-Ruel, C. Lu, G. Moriena, and G. Sciaini, Acta Crystallogr., Sect. A: Cryst. Phys., Diffr., Theor. Gen. Crystallogr. **66**, 137 (2010).
[3]C.-Y. Ruan, Y. Murooka, R. K. Raman, R. A. Murdick, R. J. Worhatch, and A. Pell, Microsc. Microanal. **15**, 323 (2009).
[4]S. Williamson, G. Mourou, and J. C. M. Li, Phys. Rev. Lett. **52**, 2364 (1984).
[5]B. J. Siwick, J. R. Dwyer, R. E. Jordan, and R. J. D. Miller, Science **302**, 1382 (2003).
[6]S. Nie, X. Wang, H. Park, R. Clinite, and J. Cao, Phys. Rev. Lett. **96**, 025901 (2006).
[7]P. Musumeci, J. T. Moody, C. M. Scoby, M. S. Gutierrez, M. Westfall, and R. K. Li, J. Appl. Phys. **108**, 114513 (2010).
[8]D.-S. Yang, N. Gedik, and A. H. Zewail, J. Phys. Chem. C **111**, 4889 (2007).
[9]P. Baum, D.-S. Yang, and A. H. Zewail, Science **318**, 788 (2007).
[10]B. Barwick, H. S. Park, O.-H. Kwon, J. S. Baskin, and A. H. Zewail, Science **322**, 1227 (2008).
[11]A. Yurtsever and A. H. Zewail, Science **326**, 708 (2009).
[12]O.-H. Kwon and A. H. Zewail, Science **328**, 1668 (2010).
[13]B. Barwick, D. J. Flannigan, and A. H. Zewail, Nature **462**, 902 (2009).
[14]A. Ichimiya and P. I. Cohen, *Reflection High Energy Electron Diffraction* (Cambridge University Press, Cambridge, 2004).
[15]Z. L. Wang, *Elastic and Inelastic Scattering in Electron Diffraction and Imaging* (Plenum, New York, 1995).
[16]Z. L. Wang, *Reflection Electron Microscopy and Spectroscopy for Surface Analysis* (Cambridge University Press, Cambridge, 1996).
[17]C.-Y. Ruan, F. Vigliotti, V. A. Lobastov, S. Chen, and A. H. Zewail, Proc. Natl. Acad. Sci. U.S.A. **101**, 1123 (2004).
[18]G. Mourou and S. Williamson, Appl. Phys. Lett. **41**, 44 (1982).
[19]A. Gahlmann, S. T. Park, and A. H. Zewail, Phys. Chem. Chem. Phys. **10**, 2894 (2008).
[20]P. Baum and A. H. Zewail, Proc. Natl. Acad. Sci. U.S.A. **103**, 16105 (2006).
[21]H. Park and J. M. Zuo, Appl. Phys. Lett. **94**, 251103 (2009).
[22]S. Schäfer, W. Liang, and A. H. Zewail, Chem. Phys. Lett. **493**, 11 (2010).
[23]W. Liang, S. Schäfer, and A. H. Zewail (unpublished).
[24]A. Ichimiya, Jpn. J. Appl. Phys. **22**, 176 (1983).
[25]A. Ichimiya, Surf. Sci., **235**, 75 (1990).
[26]A. Ichimiya, S. Kohmoto, H. Nakahara, and Y. Horio, Ultramicroscopy **48**, 425 (1993).
[27]P. A. Doyle and P. S. Turner, Acta Crystallogr., Sect. A: Cryst. Phys., Diffr., Theor. Gen. Crystallogr. **24**, 390 (1968).
[28]J. M. Zuo, M. Kim, M. O'Keeffe, and J. C. H. Spence, Nature **401**, 49 (1999).

[29]S. L. Dudarev, L. M. Peng, and M. J. Whelan, Surf. Sci. **330**, 86 (1995).
[30]U. Korte and G. Meyer-Ehmsen, Surf. Sci. **298**, 299 (1993).
[31]U. Korte and G. Meyer-Ehmsen, Phys. Rev. B **48**, 8345 (1993).
[32]M. Trigo, J. Chen, V. H. Vishwanath, Y. M. Sheu, T. Graber, R. Henning, and D. A. Reis, Phys. Rev. B **82**, 235205 (2010).
[33]A. Yurtsever and A. H. Zewail (unpublished).
[34]S. I. Anisimov, B. L. Kapeliovich, and T. L. Perelman, Sov. Phys. JETP **39**, 375 (1974).
[35]Since the lateral profile of the excitation laser is much larger than the penetration depth within the sample, only the direction z perpendicular to the surface has to be considered.
[36]The lattice heat conductivity can be generally neglected in metals.
[37]*CRC Handbook of Chemistry and Physics*, 85th ed., edited by D. Lide (CRC, Boca Raton, FL, 2005).
[38]J. Hohlfeld, S. S. Wellershoff, J. Güdde, U. Conrad, V. Jähnke, and E. Matthias, Chem. Phys. **251**, 237 (2000).
[39]Z. Lin and L. V. Zhigilei, Appl. Surf. Sci. **253**, 6295 (2007).
[40]Z. Lin, L. V. Zhigilei, and V. Celli, Phys. Rev. B **77**, 075133 (2008).
[41]H. E. Elsayed-Ali and P. M. Weber, "Time-resolved surface electron diffraction," in *Time-resolved Diffraction*, edited by J. R. Helliwell and P. M. Rentzepis (Oxford Science Publications, New York, 1997).
[42]K. J. Tilli, A. Tiitta, and H. Pöyry, Acta Crystallogr., Sect. A: Cryst. Phys., Diffr., Theor. Gen. Crystallogr. **36**, 253 (1980).
[43]W. Wendelen, A. A. Dzhurakhalov, F. M. Peeters, and A. Bogaerts, J. Phys. Chem. C **114**, 5652 (2010).
[44]J. Tang, D.-S. Yang, and A. H. Zewail, J. Phys. Chem. C **111**, 8957 (2007).
[45]D. S. Ivanov and L. V. Zhigilei, Phys. Rev. B **68**, 064114 (2003).
[46]Z. Lin and L. V. Zhigilei, J. Phys.: Conf. Ser. **59**, 11 (2007).
[47]J. Li, R. Clinite, X. Wang, and J. Cao, Phys. Rev. B **80**, 014304 (2009).
[48]X. Wang, S. Nie, J. Li, R. Clinite, M. Wartenbe, M. Martin, W. Liang, and J. Cao, Appl. Phys. Lett. **92**, 121918 (2008).
[49]L. Verlet, Phys. Rev. **159**, 98 (1967).
[50]Minor differences can be attributed to inelastic scattered electrons, inhomogeneities of the sample surface and inaccuracies in experimentally varying θ and ϕ.
[51]R. Vincent and P. Midgley, Ultramicroscopy **53**, 271 (1994).
[52]W. Braun, *Applied RHEED: Reflection High-Energy Electron Diffraction During Crystal Growth*, Springer Tracts in Modern Physics Vol. 156 (Springer, Heidelberg, 1999).
[53]F. Carbone, P. Baum, P. Rudolf, and A. H. Zewail, Phys. Rev. Lett. **100**, 035501 (2008).
[54]J. B. Pendry, *Low Energy Electron Diffraction: The Theory and Its Application to Determination of Surface Structures* (Academic, New York, 1974).
[55]M. van Hove, W. Weinberg, and C.-M. Chan, *Low-Energy Electron Diffraction: Experiment, Theory, and Surface Structure Determination* (Springer-Verlag, Berlin, 1986).
[56]E. Conrad, "Diffraction methods," in *Handbook of Surface Science Vol 1: Physical Structure*, edited by W. N. Unertl (Elsevier, New York, 1996).
[57]The proper theoretical framework to include, e.g., defects in multiple scattering simulations for RHEED is not fully understood [see also P. A. Maksym, Surf. Sci. **493**, 1 (2001)].
[58]Structural changes within the unit cell and without changing the unit cell dimensions can be observed on a shorter time scale.
[59]S. Schäfer, W. Liang, and A. H. Zewail, New J. Phys. **13**, 063030 (2011).
[60]K. Komatsu and T. Nagamiya, J. Phys. Soc. Jpn. **6**, 438 (1951).
[61]R. Chen and P. Trucano, Acta Crystallogr. Sect. A: Cryst. Phys., Diffr., Theor. Gen. Crystallogr. **34**, 979 (1978).
[62]T. Nihira and T. Iwata, Phys. Rev. B **68**, 134305 (2003).
[63]R. G. Musket, W. McLean, C. A. Colemenares, D. M. Makowiecki, and W. J. Siekhaus, Appl. Surf. Sci. **10**, 143 (1982).
[64]The remaining intensity variation near the sulfur transition energy is due to diffraction effects.